Nano Research

ISSN 1998-0124 CN 11-5974/O4
https://doi.org/10.1007/s12274-021-3893-y

Research Article

Microwave synthesis of single-phase nanoparticles made of multi-principal element alloys

Siyu Wu[1], Yuzi Liu[2], Yang Ren[3], Qilin Wei[1], and Yugang Sun[1] (✉)

[1] *Department of Chemistry, Temple University, 1901 North 13th Street, Philadelphia, Pennsylvania 19122, USA*
[2] *Center for Nanoscale Materials, Argonne National Laboratory, 9700 South Cass Avenue, Lemont, Illinois 60439, USA*
[3] *X-ray Science Division, Advanced Photon Source, Argonne National Laboratory, 9700 South Cass Avenue, Lemont, Illinois 60439, USA*

Received: 8 July 2021 / **Revised:** 21 August 2021 / **Accepted:** 16 September 2021

ABSTRACT

Metal nanoparticles of multi-principal element alloys (MPEA) with a single crystalline phase have been synthesized by flash heating/cooling of nanosized metals encapsulated in micelle vesicles dispersed in an oil phase (e.g., cyclohexane). Flash heating is realized by selective absorption of a microwave pulse in metals to rapidly heat metals into uniform melts. The oil phase barely absorbs microwave and maintains the low temperature, which can rapidly quench the high-temperature metal melts to enable the flash cooling process. The precursor ions of four metals, including Au, Pt, Pd, and Cu, can be simultaneously reduced by hydrazine in the aqueous solution encapsulated in the micelle vesicles. The resulting metals efficiently absorb microwave energy to locally reach a temperature high enough to melt themselves into a uniform mixture. The duration of microwave pulse is crucial to ensure the reduced metals mix uniformly, while the temperature of oil phase is still low to rapidly quench the metals and freeze the single-phase crystalline lattices in alloy nanoparticles. The microwave-enabled flash heating/cooling provides a new method to synthesize single-phase MPEA nanoparticles of many metal combinations when the appropriate water-in-oil micelle systems and the appropriate reduction reactions of metal precursors are available.

KEYWORDS

microwave synthesis, flash heating and cooling, high-entropy alloys, quaternary alloys, metal nanoparticles

1 Introduction

Multi-principal element alloy (MPEA) nanoparticles with pure crystalline phase, comparing to their counterpart monometallic nanoparticles, are attracting research interest in various disciplines such as catalysis [1, 2]. For example, alloying one expensive metal with the second, third, and even more metal elements not only lowers the use of the most expensive metal, but also provides an effective way to tune the electronic structures of the alloys from the possible thousands of metal combinations [3, 4]. With respect to heterogeneous catalysis, theoretical modeling and computations have frequently predicted the enhancement of catalytic activity at heterometallic sites [5, 6], but the experimental attempts of uniformly mixing multiple metal elements to form alloys with single crystalline phases are still challenging [7–9]. The difficulty mainly originates from the thermodynamic immiscibility of different metal elements, which usually leads to phase segregation in nanoparticles during synthesis. When the metal combinations exhibit good miscibility across a wide range of concentration, single-phase alloy nanoparticles have been readily synthesized from different methods including colloidal chemical synthesis [10–12]. In contrast, the metal combinations with low miscibility tend to form phase-segregated nanoparticles such as core–shell nanoparticles with cores and shells of different compositions and multi-domain nanoparticles [13, 14], which are thermodynamically stable than the single-phase alloy nanoparticles with uniform distribution of individual elements. Kinetics control over the formation of nanoparticles represents an effective strategy to overcome the thermodynamic limitation, enabling the synthesis of single-phase MPEA nanoparticles made of immiscible elements. For example, Yao et al. reported a carbothermal shock synthesis of single-phase MPEA nanoparticles, in which the corresponding solid-state metal salt mixtures on carbon nanofiber supports were decomposed to metals and melted into nanosized liquid droplets of metal mixtures upon electrically thermal shock up to a temperature of ~ 2,000 K in the period of 55 ms (i.e., rate of ~ 10^5 K/s) [15]. Despite the high tendency to coarsening into large droplets of the melted metals, the inhomogeneity of surface chemistry of the carbon nanofibers, i.e., metal non-wettable carbon vs. metal-affinitive surface-bound oxygen (O^*) residuals, forced the liquid metals to shatter into nanosized droplets that strongly bonded to the surface sites with O^*. The following ultrafast cooling at an appropriate rate (~ 10^5 K/s) solidified individual liquid droplets to form single-phase alloy nanoparticles. The high cooling rate plays a crucial role in determining the crystalline phases of the resulting nanoparticles. However, rapid heating and rapid cooling are challenging to achieve in colloidal chemistry because temperature control of reaction solutions in conventional reactors (e.g., glass flask, autoclave, etc.) relies on heat diffusion between the entire reactors and external heating source. Such globalized heating strategy cannot support rapid temperature increase to the values for melting metals while the solvents and reactors are still safe.

Address correspondence to ygsun@temple.edu

Therefore, selective heating of metal components in liquid phase becomes crucial to enabling the synthesis of single-phase MPEA nanoparticles.

Both high-power pulsed laser [16, 17] and microwave radiation [18, 19] are capable of selectively heating metals dispersed in appropriate solvents. In this work, high-power microwave radiation is used as the external energy source for selectively heating metal components including metal precursor ions in reaction solutions because of its potential in scalable synthesis [20, 21]. Bulk metals with smooth surfaces usually reflect microwave radiation, but the absorption of microwave radiation in metal nanoparticles becomes significant because of their high surface curvatures and large refractive indices, which strongly depend on dimensions of the materials [22, 23]. The efficient absorption of microwave radiation in nanosized metals and metal precursor ions will enable selective flash heating of the chemically produced metals upon exposure to a high-power microwave pulse when metal nanoparticles are synthesized in a solvent that is transparent to the microwave. When the microwave power is strong enough and the pulse duration is long enough, the produced metals melt while the solvent still maintains a low temperature, creating a significant temperature gradient between the melted metals and the surrounding solvent. Once the microwave irradiation is turned off, the melted metals (or liquid metals) are rapidly quenched by dissipating heat to the solvent, forming single-phase MPEA nanoparticles. Micelle vesicles *in-situ* formed from microemulsion process are used as transient nanoreactors to physically confine the liquid metals, generating nanosized metal solids. We recently evaluated the microwave-enabled flash-heating and flash-cooling strategy by synthesizing single-phase PtAu alloy nanoparticles with arbitrary ratios of the two thermodynamically immiscible elements using water-in-oil micelles as nanoreactor [24]. In this work, the microwave-enabled flash-heating and flash-cooling method is extended to synthesize single-phase MPEA nanoparticles containing four elements of Au, Pt, Pd, and Cu (see Fig. S1 in the Electronic Supplementary Material (ESM) for their miscibility), shedding light on the promise in synthesizing single-phase MPEA nanoparticles with complex compositions.

2 Experimental

In a typical synthesis of single-phase AuPtPdCu MPEA nanoparticles, a stocked oil-phase suspension was prepared by mixing 48 mL cyclohexane, 8 mL n-butanol, and 4 g cetyltrimethylammonium bromide (CTAB) under ultrasonic vibrations for 30 min until the two-phase system turned milky white. The solution **I** containing metal precursors was obtained by adding 20 μL of aqueous solution of each metal precursor (0.1 M) into 2 mL stocked hexane/butanol/CTAB suspension. The metal precursor chemicals were $HAuCl_4$, Na_2PtCl_4, Na_2PdCl_4, and $CuCl_2$ for producing Au, Pt, Pd, and Cu, respectively. A clear dispersion was obtained after 15-min sonication, indicating the formation of water-in-oil microemulsion micelle vesicles. The metal precursors were enclosed in the micelle vesicles. The solution **II** containing reducing agent was prepared in a same procedure except the addition of 80-μL hydrazine hydrate (64% hydrazine). Hydrazine was also enclosed in the micelle vesicles. The solution **I** containing metal precursors was frozen into a wax-like solid in a freezer set at −20 °C because the freezing point of cyclohexane was 6.5 °C. When the solution **II** was added to the frozen solution **I**, the liquid-state solution **II** was above the solid-state solution **I** at room temperature. The solution **I** and solution **II** were well separated to prevent the reduction of metal precursors. The two-layer solution in a microwave reaction tube was then placed in an Anton Paar Monowave 300 microwave reactor equipped with a 2.45 GHz microwave generator of 850 W in power. Turning on the microwave selectively heated the aqueous solution in the micelle vesicles in both solution **I** and **II**, broken the micelle vesicles, mixed solution **I** and **II**, formed new micelle vesicles containing both metal precursors and hydrazine, and triggered reduction reaction of metal precursors to produce metals. Note: The large volume oil phase barely absorbed microwave energy to increase temperature although the metals enclosed in the micelle vesicle might be at very high temperature. During 10-s microwave heating at the maximum power, the global temperature of the solution (dominated by cyclohexane) was monitored with the internal contactless infrared (IR) detector, showing the reading change from ~ 0 to ~ 70 °C. Once the microwave was turned off, strong airflow was applied to cool the solution quickly down to room temperature, avoiding the possible spill caused by solvent boiling. The metal nanoparticles were collected by centrifugation followed by washing with ethanol and water three times. A more detailed description of chemicals, synthesis, and characterizations can be found in the ESM.

3 Results and discussion

When a high-power microwave pulse is applied to the two-layer micelle solution, cyclohexane (oil phase) with loss tangent (tanδ) of < 0.0001 is transparent to microwave and barely absorbs microwave radiation. In contrast, the water phase containing metal ions is encapsulated in the micelle vesicles quickly and efficiently absorbs the microwave energy because of their high loss tangents (i.e., 0.12 and 0.57 for water and n-butanol molecules, respectively). The non-uniform heating, i.e., selective heating of the micelle-encapsulated water phase, leads to vigorous agitation of the mixed solution. The solution agitation facilitates quick fusion of the two types of micelles (i.e., ones containing metal precursors and ones containing hydrazine) and the formation of new micelles containing both hydrazine and metal precursor ions, triggering the rapid reduction of metal ions to produce metal atoms. The metal atoms condense to nanosized solid particles or liquid droplets, which possess free electrons to be resonant with microwave to absorb microwave energy more efficiently [25, 26]. The conversion of microwave energy to heat in the nanosized metals can locally maintain temperature high enough to keep the nanosized metals in liquid or quasi-liquid state, enabling the uniform mixing of all elements in each nanosized droplet. When the microwave is turned off, the high temperature gradient between the liquid metals and the surrounding cyclohexane quenches the liquid metals, lowering their temperature rapidly to solidify them into alloy nanoparticles while maintaining the uniform element distribution same as in the liquid metals. The rapid quenching kinetics, i.e., fast enough temperature decrease rate, is crucial to freeze the uniform element distribution of the liquid metals to form single-phase MPEA nanoparticles.

Figure 1(a) shows a typical transmission electron microscopy (TEM) image of the AuPtPdCu MPEA nanoparticles synthesized from a reaction with a 10 s microwave pulse. The molar ratio of the metal precursors, i.e., $HAuCl_4$, Na_2PdCl_4, Na_2PtCl_4, and $CuCl_2$, is 1:1:1:1. The nanoparticles exhibit an average size of 6.1 nm with a standard deviation of 1.2 nm (Fig. 1(b)). The granular nanoparticles exhibit narrow size distribution. The nanoparticles are not well separated or somehow connected with neighboring ones (Figs. S2(a) and S2(b) in the ESM), which can be ascribed to that the quenching kinetics might be not fast enough to completely shatter liquid metals and solidify them into well-separated nanoparticles on the inner walls of the micelle vesicles. Ultrasonication of the as-synthesized nanoparticles in water cannot disperse them into freestanding individual ones, indicating

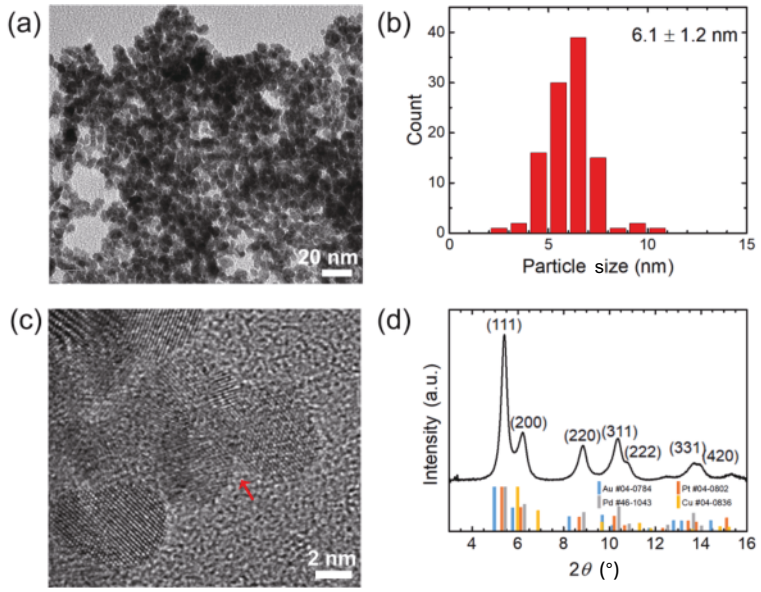

Figure 1 Characterization of the synthesized single-phase AuPtPdCu MPEA nanoparticles. (a) TEM image of the nanoparticles dispersed on a TEM grid. (b) Particle size distribution statistics according to the dimensions measured from the TEM image. (c) HR-TEM image of a cluster of nanoparticles connected by thin bottlenecks, which are indicated by the red arrow. (d) HE-XRD pattern of the nanoparticles. The sticks coded with different colors refer to the standard XRD patterns of pure metal powders. The wavelength of X-ray was 0.2115 Å (corresponding to photon energy of 58.621 keV).

the physical connections between neighboring nanoparticles. High-resolution TEM (HR-TEM) image of a cluster of nanoparticles shows the existence of thin bottlenecks that fuse the adjacent nanoparticles (Fig. 1(c)). The two adjacent nanoparticles linked by one bottleneck exhibit different crystalline orientations, indicating that the nanoparticles are formed independently during the rapid temperature quenching. When the liquid metals shatter and solidify into nanoparticles, the residual liquid metals between neighboring nanoparticles solidify to form the bottlenecks. Energy-dispersive X-ray spectroscopy (EDX) of ensembled nanoparticles in a scanning electron microscopy (SEM) sample shows the presence of all four metal elements (i.e., Au, Pt, Pd, and Cu) in the synthesized nanoparticles (Figs. S2(c) and S2(d) in the ESM). The semi-quantitative analysis of fitting the EDX peaks gives the atomic percentage of each element in the nanoparticles, i.e., 25%, 17%, 23%, and 35% for Au, Pt, Pd, and Cu, respectively (see Table S2 in the ESM). Accurate elemental analysis of the nanoparticle dispersion using inductively coupled plasma optical emission spectroscopy (ICP-OES) determines the atomic percentage of each element as 29%, 15%, 28%, and 28% for Au, Pt, Pd, and Cu, respectively (or a formula of $Au_{0.29}Pt_{0.15}Pd_{0.28}Cu_{0.28}$). The compositions determined by these two measurements agree well except that Cu weighs more in the EDX analysis, indicating that EDX analysis can be used to quickly estimate the compositions of synthesized nanoparticles with reasonable accuracy. It is worth noting that Pt in the synthesized nanoparticles exhibits a lower concentration compared with the concentration of the corresponding precursor (Na_2PtCl_4) in the reaction solution. Such a deviation might originate from the self-decomposition of the stocked Na_2PtCl_4 solution, which leads to the formation of precipitates and lowers the actual concentration of $PtCl_4^{2-}$ ions in the solution. The other three elements, i.e., Au, Pd, and Cu, exhibit 1:1:1 atomic ratio in the nanoparticles, consistent with the molar ratio of their corresponding precursors in the reaction solution.

High-energy X-ray diffraction (HE-XRD) pattern of the nanoparticles exhibits peaks corresponding to only one set of face-centered cubic (fcc) lattice, indicating the single crystalline phase of the synthesized MPEA nanoparticles (Fig. 1(d)). The absence of peak splitting confirms the exclusion of phase segregation during rapid quenching the liquid metals. The peaks located at 5.409°, 6.204°, and 8.839° correspond to (111), (200), and (220) reflections, respectively. According to Bragg's equation, the interplanar distances (d) between (111), (200), and (220) crystalline planes are 2.242, 1.954, and 1.371 Å, respectively (Tables S3 and S4 in the ESM). The (111) peak of the single-phase AuPtPdCu MPEA nanoparticles falls between the peaks of the pure Au metal with the largest unit cell (5.147°, JCPDF #04-0784) and the pure Cu metal with the smallest unit cell (5.806°, JCPDF #04-0836). It is close to that of pure Pt metal (5.352°, JCPDF #04-0802) and pure Pd metal (5.398°, JCPDF #46-1043).

Elemental distribution of four metal elements in individual nanoparticles has been characterized with high-angle annular dark-field scanning TEM (HAADF-STEM) coupled with EDX mapping (Fig. 2). All four elements are present in each nanoparticle (Figs. 2(b)–2(e)). The spatial distributions of all elements overlap very well, confirming the homogeneous mixing of all four elements in the single-phase MPEA nanoparticles (Fig. 2(f)). The enlarged HAADF-STEM/EDX maps (Fig. S3 in the ESM) of the bottlenecks between neighboring nanoparticles show higher concentration of Pd in the bottlenecks than nanoparticles, as evidenced by the bluer color of the bottlenecks than the nanoparticles (Fig. 3(a)). The enrichment of Pd in the bottlenecks implies that the different Pd concentrations in the bottlenecks and adjacent nanoparticles do not generate significant difference in lattice constant to break the (unnecessary) connection of neighboring MPEA nanoparticles. The (111) interplanar distance of pure Pd metal is 2.246 Å, which is almost the same as that of the MPEA nanoparticles (i.e., 2.242 Å). The lattice matching between the bottlenecks and neighboring MPEA nanoparticles represents the thermodynamic driving force to bridge MPEA nanoparticles with the bottlenecks because the temperature quenching kinetics is not rapid enough to completely shatter liquid metals into well-separated nanoparticles. The HR-TEM image of a Pd-enriched bottleneck shows that its lattice continuously extends from the lattices of neighboring MPEA nanoparticles (Fig. 3(b)). Because of the thin thickness, the lattice of the bottleneck distorts with nonparallel (111) lattice fringes in a radial angle range of ~ 12°. The existence of lattice distortion and high-entropy metal mixing in the synthesized nanoparticles may induce peak broadening in the HE-XRD pattern. According to Scherrer's equation, the uniform nanoparticles with size of 6.1 nm should exhibit (111) XRD peak with a full width at half maximum

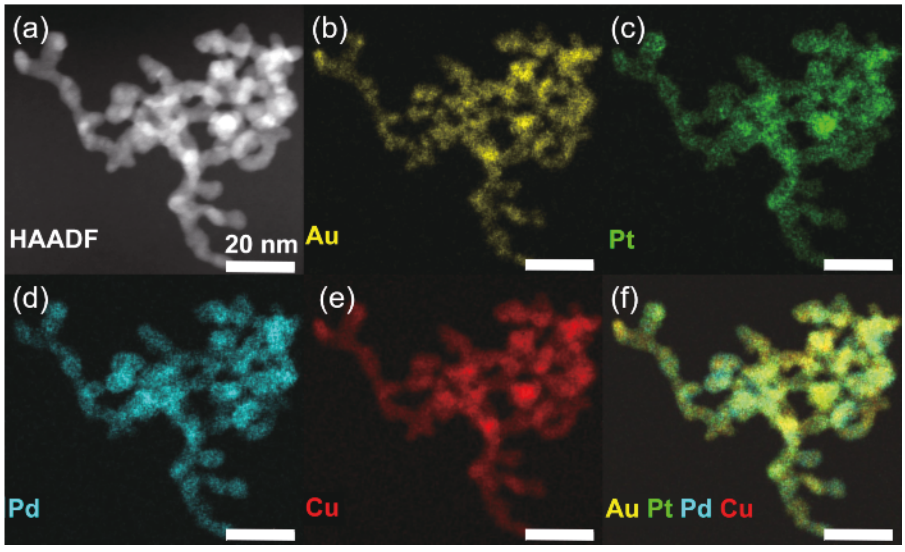

Figure 2 (a) HAADF-STEM image and ((b)–(e)) elemental EDX mappings of (b) Au, (c) Pt, (d) Pd, and (e) Cu of the synthesized single-phase AuPtPdCu nanoparticles. (f) Overlaid images of the elemental EDX mapping are shown in ((b)–(e)). The scale bar in (a) also is applies to ((b)–(f)).

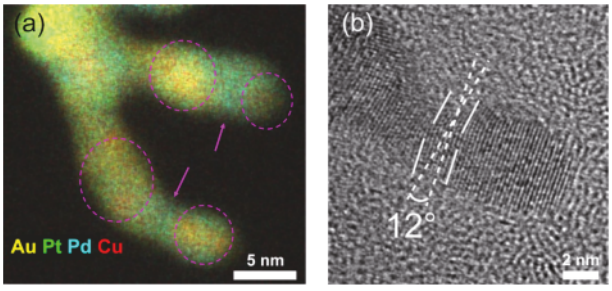

Figure 3 (a) Overlaid EDX mapping images of Au, Pt, Pd, and Cu of connected nanoparticles, highlighting the non-uniform composition in the bottlenecks (indicated by arrows) and nanoparticles (indicated by the dashed circles). The bluer color (coded for Pd) of the bottlenecks indicates higher concentration of Pd in the bottlenecks than in the nanoparticles. (b) HR-TEM image of two nanoparticles connected with a thinner bottleneck that exhibits a minor angular lattice distortion.

(fwhm) of 0.188°. The fwhm of (111) peak measured from the synthesized AuPtPdCu MPEA nanoparticles is 0.31°, confirming the peak broadening effect (Table S3 in the ESM).

The successful synthesis of single-phase AuPtPdCu MPEA nanoparticles confirms the ability of the microwave-enabled flash-heating/flash-cooling in homogeneously mixing the immiscible elements. This synthesis protocol is also feasible to synthesize single-phase MPEA nanoparticles made of ternary element combinations (i.e., AuPtPd, AuPtCu, AuPdCu, and PtPdCu). TEM images of these ternary MPEA nanoparticles show the morphology similar to that of the quaternary AuPtPdCu MPEA nanoparticles (Figs. S4–S7 in the ESM, frames (a) and (b)). The average sizes of the ternary MPEA nanoparticles are 7.1 ± 1.9, 6.5 ± 1.3, 7.2 ± 1.9, and 5.9 ± 1.1 nm for AuPtPd, AuPtCu, AuPdCu, and PtPdCu nanoparticles, respectively (Figs. S4–S7 in the ESM, frames (c)). The EDX spectrum of each sample confirms the existence of the corresponding three metal elements (Figs. S4–S7 in the ESM, frames (d); Table S5–S8 in the ESM). The chemical formulae of these ternary MPEA nanoparticles, determined with ICP-OES measurement, are calculated as $Au_{0.38}Pt_{0.20}Pd_{0.42}$, $Au_{0.50}Pt_{0.16}Cu_{0.34}$, $Au_{0.37}Pd_{0.31}Cu_{0.32}$, and $Pt_{0.20}Pd_{0.48}Cu_{0.32}$, respectively.

The HE-XRD patterns of the ternary MPEA nanoparticles are consistent with the fcc lattices of one group of well-defined (111), (200), and (220) peaks regardless of the compositions (Fig. S8, Tables S3 and S4 in the ESM). The positions of XRD peaks (or the interplanar distance) shift with the variation of the average size of the metal atoms in the alloy nanoparticles. For example, the (111) peak shifts from 5.297° for the AuPtPd nanoparticles (without the smallest Cu atoms) to 5.543° for the PtPdCu nanoparticles (without the largest Au atoms) (blue curve versus cyan curve, Fig. 4(a)). According to the empirical Vegard's law, the lattice constant (or a specific interplanar distance) of an alloy is determined from the linear combination of the lattice constant (or a specific interplanar distance) of each pure element weighted by its atomic fraction

$$a = x_A a_A + x_B a_B + \cdots + x_Z a_Z$$

where x is the atom fraction, a is the lattice constant or a specific interplanar distance, and the subscripts represent the elements. The (111) interplanar distances (d_{111}) of pure Au, Pt, Pd, and Cu

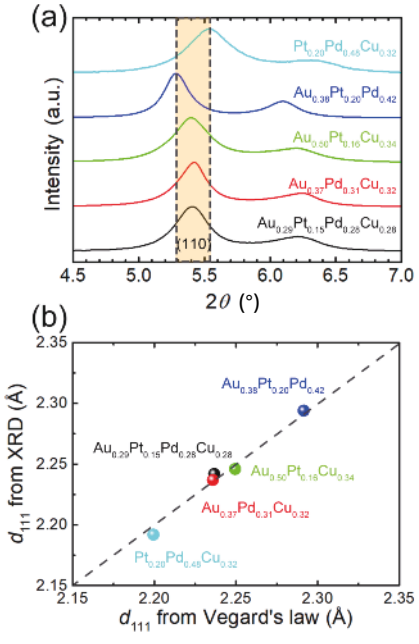

Figure 4 (a) HE-XRD patterns of the synthesized single-phase MPEA nanoparticles made of $Au_{0.29}Pt_{0.15}Pd_{0.28}Cu_{0.28}$, $Au_{0.37}Pd_{0.31}Cu_{0.32}$, $Au_{0.50}Pt_{0.16}Cu_{0.34}$, $Au_{0.38}Pt_{0.20}Pd_{0.42}$, and $Pt_{0.20}Pd_{0.48}Cu_{0.32}$, scaled to show the (110) and (200) diffraction peaks only. (b) The interplanar distance along [111] direction, i.e., d_{111}, determined from the HE-XRD patterns (y-axis) is consistent with d_{111} calculated from the composition of nanoparticles according to Vegard's law (x-axis).

metals are 2.355, 2.265, 2.246, and 2.088 Å, respectively. The values of d_{111} calculated for the synthesized single-phase MPEA nanoparticles are 2.237, 2.236, 2.249, 2.291, and 2.199 Å for $Au_{0.29}Pt_{0.15}Pd_{0.28}Cu_{0.28}$, $Au_{0.37}Pd_{0.31}Cu_{0.32}$, $Au_{0.50}Pt_{0.16}Cu_{0.34}$, $Au_{0.38}Pt_{0.20}Pd_{0.42}$, and $Pt_{0.20}Pd_{0.48}Cu_{0.32}$, respectively. The calculated d_{111} agrees well with the d_{111} determined from the HE-XRD patterns (Fig. 4(b)), again confirming the uniform mixing of all elements in the synthesized MPEA nanoparticles. Since Au and Cu exhibit the largest and smallest atom size, respectively, in this group of coinage metals (i.e., Au, Pt, Pd, and Cu), d_{111} of the MPEA nanoparticles are mainly determined by the atom ratio of Au:Cu. For instance, the MPEA nanoparticles without either Au or Cu, i.e., $Pt_{0.20}Pd_{0.48}Cu_{0.32}$ and $Au_{0.38}Pt_{0.20}Pd_{0.42}$, exhibit d_{111} of 2.192 and 2.294 Å, representing ~ 5% difference in lattice constant. Controlling the composition of single-phase MPEA nanoparticles is effective to tune lattice constant to influence their properties such as catalysis [27].

The global temperature of solution (dominated by the oil-phase cyclohexane) and pressure above the solution during the nanoparticle synthesis can be monitored in real time using the build-in contactless IR thermometer and pressure gauge. The real-time change of both temperature and pressure has been recorded from a typical synthesis of MPEA AuPtPdCu nanoparticles, and the results are presented in Fig. 5(a). Once the microwave pulse is turned on, microwave radiation is mainly absorbed by the water phase containing metal precursors and reduced metals encapsulated in the micelle vesicles, resulting in rapid temperature increase locally. In the 10-s course of microwave pulse, the global temperature increases from ~ 0 to ~ 70 °C. The temperature continues increasing to ~ 80 °C after the microwave is turned off, confirming that the water phase and metals are locally heated to higher temperatures. The post-microwave temperature increase lasting ~ 5 s indicates that the metal phase is very hot and possesses significant amount of heat. In contrast, a controlling experiment is conducted with the oil-phase only (i.e., the cyclohexane/CTAB/1-butanol mixture without metal precursors and hydrazine in micelle vesicles). A 10-s microwave heating increases the temperature from ~ 0 only to ~ 30 °C, and the temperature stops increasing immediately after turning off the microwave. The comparison clearly shows that the metal precursors and metals formed from the reduction reaction represent the hot spots in the synthesis solution to efficiently absorb the microwave radiation and rapidly increase their temperatures locally. The rapid local heating is essential to promote the fast reduction of metal precursors and melt the reduced metals to a liquid or quasi-liquid state.

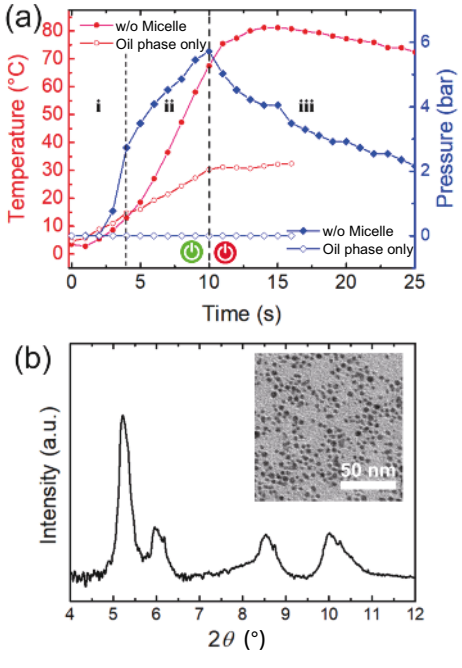

Figure 5 (a) Time-dependent variation of global temperature of the synthesis solution measured with the internal IR thermometer (solid red dots) and pressure above the solution (solid blue diamonds) under a 10-s microwave pulse. The data recorded for a solution without micelles (i.e., absence of water, metal precursors, and hydrazine) are presented as reference (hollow symbols). (b) The HE-XRD pattern and TEM image (inset) of alloy nanoparticles containing Au, Pt, Pd, and Cu synthesized with a 3-s microwave pulse.

Heating the oil-phase only with the microwave pulse does not build up any pressure in the reactor, which contrasts with the time-dependent pressure variation for the synthesis solution containing metal precursors and hydrazine. According to the change of pressure, the entire synthesis of MPEA nanoparticles can be divided into three characteristic stages. As shown in Fig. 5(a), the pressure increases rapidly in the initial 4 s (Stage i). The frozen solution **I** containing metal precursors mixes with the solution **II** containing hydrazine to trigger the vigorous reaction between the metal ions and hydrazine, resulting in the formation of nanosized metals (possibly in solid, or liquid, or quasi-liquid state) and N_2. Although the reduction of metal ions almost completes at Stage i, continuous microwave radiation can further reduce the unreacted metal ions (e.g., Cu^{2+} ions with the least oxidizing power) to release N_2. The already formed nanosized metals efficiently absorb microwave energy to rapidly increase their temperature and facilitate melting the metals. The large temperature gradient between the melted metals and the surrounding oil phase promotes heat transfer to increase the temperature of cyclohexane at Stage ii (i.e., 410 s), increasing the vapor pressure of cyclohexane. Both the continuous release of N_2 and elevation of vapor pressure of cyclohexane further increase the pressure at Stage ii although the slope is not as steep as that at Stage i. Once the microwave is turned off, the pressure starts to drop (Stage iii).

Although most metal precursor ions can be reduced at Stage i, the extended microwave heating at Stage ii is crucial to ensuring the complete reduction of Cu^{2+} and the uniform mixing of all metals in a liquid or quasi-liquid state. When a synthesis reaction is terminated at Stage i, for example, at 3 s, the HE-XRD pattern of the resultant nanoparticles exhibits asymmetric diffraction peaks (Fig. 5(b)), indicating the co-existence of two types of fcc lattices. The major set of XRD peaks locate at 5.219°, 5.956°, 8.534°, and 10.009°, corresponding to the fcc lattice with d_{111} of 2.32 Å. A secondary set of XRD peaks center at 5.34°, 6.17°, 8.74° and 10.25°, referring to the fcc lattice with a smaller d_{111} of 2.27 Å. The co-existence of two types of fcc crystalline phases might be ascribe to two possible reasons. First, the temperature of metals formed from the reduction of metal precursors at 3 s is not high enough to melt the metals to uniformly mix all elements. Second, the temperature gradient from the metals to surrounding cyclohexane is not large enough to rapidly freeze the high entropy state of melted metals but allows phase segregation. The nanoparticles formed with 3-s microwave pulse are well separated on the TEM grid (inset, Fig. 5(b)) and different from the geometry of the single-phase AuPtPdCu MPEA nanoparticles formed with 10-s microwave pulse (Fig. 1(a)), which possess bottlenecks connecting individual nanoparticles. The difference in geometries of the nanoparticles synthesized with microwave pulse of different durations indicates that the first reason could be more likely responsible for the observed two crystalline phases in the nanoparticles formed with shorter microwave pulse. In addition, the values of d_{111} of the nanoparticles formed with 3-s microwave pulse are larger than that of the single-phase AuPtPdCu MPEA nanoparticles, indicating the lack of small Cu atoms in the nanoparticles shown

in Fig. 5(b). EDX analysis of the nanoparticles gives the atomic percentages of 25%, 15%, 33%, and 27% for Au, Pt, Pd, and Cu, respectively. The EDX analysis shows a lower Cu percentage (27%) compared to that (35%) in the nanoparticles synthesized from the 10-s microwave reaction. (Note: The concentrations of each elements in the synthesized nanoparticles determined from EDX analysis are not as accurate as ICP-OES measurement because of the intrinsic inaccuracy of the quantitative analysis model. The comparison of the atomic percentages between two samples using the same EDX analysis procedure is still valid to tell the difference between the samples.) The difference of the Cu percentage in the nanoparticles synthesized from the microwave reaction of different times indicates that a short reaction time (3 s) cannot completely reduce the copper salt. Therefore, it is important to extend microwave heating to Stage ii to ensure the complete reduction of Cu^{2+} and to melt the metals into uniform metal mixture. When the microwave is turned off at Stage iii, the uniform metal melts are rapidly quenched by surrounding cyclohexane to solidify into single-phase MPEA nanoparticles. The volume shrinking during the solidification process shatters the metal melts into smaller nanoparticles. The incomplete separation of individual nanoparticles might be owing to that the temperature gradient cannot induce rapid enough quenching of the metal melts and/or that the interaction between the metals and the inner wall of micelle vesicles is too strong to prevent volume shrinking of the metals.

In summary, single-phase MPEA nanoparticles made of quaternary and ternary metal elements have been successfully synthesized by the method relying on microwave-enabled flash heating/flash cooling of nanosized metals in micelle vesicles dispersed in microwave-transparent cyclohexane (oil phase). The microscopic characterizations including HR-TEM imaging and EDX mapping confirm the uniform distribution of all elements and pure fcc lattice in individual nanoparticles. A long enough duration of microwave pulse is crucial to ensure that the metals formed from reduction of metal precursor ions can be melted to mix all elements homogeneously, facilitating the formation of single crystalline phase during the rapid temperature quenching. The synthesis protocol reported in this work is ready to synthesize single-phase MPEA nanoparticles of other compositions when appropriate metal precursors, reductants, micelle surfactants, and power and duration of microwave pulse are optimized. The future study of the alloy structure and structure-related physical and chemical properties of single-phase MPEA nanoparticles with various of compositions will generate a large pool for selecting high mechanical perforamce alloys [28] as well as high-performance catalysts towards various of reactions [29].

Acknowledgements

This work was supported by the National Science Foundation (NSF) of United States under NSF award (No. 1946912). Materials characterizations were partially performed at Temple Materials Institute (TMI). Use of the Center for Nanoscale Materials, an Office of Science user facility, was supported by the U.S. Department of Energy, Office of Science, Office of Basic Energy Sciences, under Contract No. DE-AC02-06CH11357. This research used resources of the Advanced Photon Source, a U.S. Department of Energy (DOE) Office of Science User Facility, operated for the DOE Office of Science by Argonne National Laboratory under Contract No. DE-AC02-06CH11357.

Electronic Supplementary Material: Supplementary material (materials synthesis and characterization, Figs. S1–S8 and Tables S1–S8) is available in the online version of this article at https://doi.org/10.1007/s12274-021-3893-y.

References

[1] Toshima, N.; Yonezawa, T. Bimetallic nanoparticles—Novel materials for chemical and physical applications. *New J. Chem.* **1998**, *22*, 1179–1201.

[2] Sharma, G.; Kumar, A.; Sharma, S.; Naushad, M.; Dwivedi, R. P.; Alothman, Z. A.; Mola, G. T. Novel development of nanoparticles to bimetallic nanoparticles and their composites: A review. *J. King Saud Univ. Sci.* **2019**, *31*, 257–269.

[3] Antolini, E.; Salgado, J. R. C.; Gonzalez, E. R. The methanol oxidation reaction on platinum alloys with the first row transition metals: The case of Pt-Co and -Ni alloy electrocatalysts for DMFCs: A short review. *Appl. Catal. B Environ.* **2006**, *63*, 137–149.

[4] Antolini, E.; Salgado, J. R. C.; Gonzalez, E. R. The stability of Pt-M (M = first row transition metal) alloy catalysts and its effect on the activity in low temperature fuel cells: A literature review and tests on a Pt-Co catalyst. *J. Power Sources* **2006**, *160*, 957–968.

[5] Lin, S. P.; Wang, K. W.; Liu, C. W.; Chen, H. S.; Wang, J. H. Trends of oxygen reduction reaction on platinum alloys: A computational and experimental study. *J. Phys. Chem. C* **2015**, *119*, 15224–15231.

[6] Li, H.; Henkelman, G. Dehydrogenation selectivity of ethanol on close-packed transition metal surfaces: A computational study of monometallic, Pd/Au, and Rh/Au catalysts. *J. Phys. Chem. C* **2017**, *121*, 27504–27510.

[7] Xiao, S.; Hu, W.; Luo, W.; Wu, Y.; Li, X.; Deng, H. Size effect on alloying ability and phase stability of immiscible bimetallic nanoparticles. *Eur. Phys. J. B Condensed Matter Complex Syst.* **2006**, *54*, 479–484.

[8] Calvo, F.; Cottancin, E.; Broyer, M. Segregation, core alloying, and shape transitions in bimetallic nanoclusters: Monte Carlo simulations. *Phys. Rev. B* **2008**, *77*, 121406.

[9] Wanjala, B. N.; Luo, J.; Fang, B.; Mott, D.; Zhong, C. J. Gold-platinum nanoparticles: Alloying and phase segregation. *J. Mater. Chem.* **2011**, *21*, 4012–4020.

[10] Gao, C. H.; Hu, Y. X.; Wang, M. S.; Chi, M. F.; Yin, Y. D. Fully alloyed Ag/Au nanospheres: Combining the plasmonic property of Ag with the stability of Au. *J. Am. Chem. Soc.* **2014**, *136*, 7474–7479.

[11] Wong, A.; Liu, Q.; Griffin, S.; Nicholls, A.; Regalbuto, J. R. Synthesis of ultrasmall, homogeneously alloyed, bimetallic nanoparticles on silica supports. *Science* **2017**, *358*, 1427–1430.

[12] Albrecht, W.; Van Der Hoeven, J. E.; Deng, T. S.; De Jongh, P. E.; Van Blaaderen, A. Fully alloyed metal nanorods with highly tunable properties. *Nanoscale* **2017**, *9*, 2845–2851.

[13] Cui, C. H.; Gan, L.; Li, H. H.; Yu, S. H.; Heggen, M.; Strasser, P. Octahedral PtNi nanoparticle catalysts: Exceptional oxygen reduction activity by tuning the alloy particle surface composition. *Nano Lett.* **2012**, *12*, 5885–5889.

[14] Long, N. V.; Hien, T. D.; Asaka, T.; Ohtaki, M.; Nogami, M. Synthesis and characterization of Pt-Pd alloy and core-shell bimetallic nanoparticles for direct methanol fuel cells (DMFCs): Enhanced electrocatalytic properties of well-shaped core-shell morphologies and nanostructures. *Int. J. Hydrogen Energy* **2011**, *36*, 8478–8491.

[15] Yao, Y. G.; Huang, Z. N.; Xie, P. F.; Lacey, S. D.; Jacob, R. J.; Xie, H.; Chen, F.; Nie, A. M.; Pu, T. C.; Rehwoldt, M. et al. Carbothermal shock synthesis of high-entropy-alloy nanoparticles. *Science* **2018**, *359*, 1489–1494.

[16] Amendola, V.; Meneghetti, M. Laser ablation synthesis in solution and size manipulation of noble metal nanoparticles. *Phys. Chem. Chem. Phys.* **2009**, *11*, 3805–3821.

[17] Amendola, V.; Polizzi, S.; Meneghetti, M. Laser ablation synthesis of gold nanoparticles in organic solvents. *J. Phys. Chem. B* **2006**, *110*, 7232–7237.

[18] Li, C. P.; Sui, J.; Zhang, Z. Q.; Jiang, X. H.; Zhang, Z. M.; Yu, L. M. Microwave-assisted synthesis of tremella-like NiCo/C composites

for efficient broadband electromagnetic wave absorption at 2–40 GHz. *Chem. Eng. J.* **2019**, *375*, 122017.

[19] Kunal, P.; Li, H.; Dewing, B. L.; Zhang, L.; Jarvis, K.; Henkelman, G.; Humphrey, S. M. Microwave-assisted synthesis of Pd_xAu_{100-x} alloy nanoparticles: A combined experimental and theoretical assessment of synthetic and compositional effects upon catalytic reactivity. *ACS Catal.* **2016**, *6*, 4882–4893.

[20] Zhu, Y. J.; Chen, F. Microwave-assisted preparation of inorganic nanostructures in liquid phase. *Chem. Rev.* **2014**, *114*, 6462–6555.

[21] Baghbanzadeh, M.; Carbone, L.; Cozzoli, P. D.; Kappe, C. O. Microwave-assisted synthesis of colloidal inorganic nanocrystals. *Angew. Chem., Int. Ed.* **2011**, *50*, 11312–11359.

[22] Zhao, X. C.; Zhang, Z. M.; Wang, L. Y.; Xi, K.; Cao, Q. Q.; Wang, D. H.; Yang, Y.; Du, Y. W. Excellent microwave absorption property of graphene-coated Fe nanocomposites. *Sci. Rep.* **2013**, *3*, 3421.

[23] Qi, X. S.; Hu, Q.; Xu, J. L.; Xie, R.; Bai, Z. C.; Jiang, Y.; Qin, S. J.; Zhong, W.; Du, Y. W. Enhanced microwave absorption properties and mechanism of core/shell structured magnetic nanoparticles/carbon-based nanohybrids. *Mater. Sci. Eng. B* **2016**, *211*, 53–60.

[24] Zhang, D. T.; Chen, C. N.; Wang, X. Y.; Guo, G. S.; Sun, Y. G. Synthesis of PtAu alloy nanocrystals in micelle nanoreactors enabled by flash heating and cooling. *Part. Part. Syst. Charact.* **2018**, *35*, 1700413.

[25] Xu, S. M.; Zhong, G.; Chen, C. J.; Zhou, M.; Kline, D. J.; Jacob, R. J.; Xie, H.; He, S. M.; Huang, Z. N.; Dai, J. Q. et al. Uniform, scalable, high-temperature microwave shock for nanoparticle synthesis through defect engineering. *Matter* **2019**, *1*, 759–769.

[26] Ano, T.; Maitani, M. M.; Sato, Y.; Tsubaki, S.; Wada, Y. Drastic microwave heating of percolated Pt metal nanoparticles supported on Al_2O_3 substrate. *Processes* **2020**, *8*, 72.

[27] Zhao, Y. G.; Wu, Y. J.; Liu, J. J.; Wang, F. Dependent relationship between quantitative lattice contraction and enhanced oxygen reduction activity over Pt-Cu alloy catalysts. *ACS Appl. Mater. Interfaces* **2017**, *9*, 35740–35748.

[28] Li, W.; Liu, P.; Liaw, P. K. Microstructures and properties of high-entropy alloy films and coatings: A review. *Mater. Res. Lett.* **2018**, *6*, 199–229.

[29] Li, Y. H.; Li, J. Y.; Xu, Y. J. Bimetallic nanoparticles as cocatalysts for versatile photoredox catalysis. *EnergyChem* **2021**, *3*, 100047.

Electronic Supplementary Material

Microwave synthesis of single-phase nanoparticles made of multi principal element alloys

Siyu Wu[1], Yuzi Liu[2], Yang Ren[3], Qilin Wei[1], and Yugang Sun[1] (✉)

[1] *Department of Chemistry, Temple University, 1901 North 13th Street, Philadelphia, Pennsylvania 19122, USA*
[2] *Center for Nanoscale Materials, Argonne National Laboratory, 9700 South Cass Avenue, Lemont, Illinois 60439, USA*
[3] *X-ray Science Division, Advanced Photon Source, Argonne National Laboratory, 9700 South Cass Avenue, Lemont, Illinois 60439, USA*

Supporting information to https://doi.org/10.1007/s12274-021-3893-y

Experiment Section

Chemicals. Cyclohexane (C_6H_{12}, 99%, Alfa Aesar), n-butanol ($C_4H_{10}O$, 99.5%, Acros Organics), cetyltrimethylammonium bromide (CTAB, 98%, Chem Impex), hydrazine hydrate ($N_2H_4H_2O$, 64%, Acros Organics), tetrachloroauric(III) acid trihydrate ($HAuCl_4 \cdot 3H_2O$, 99.9%, Alfa Aesar), sodium tetrachloroplatinate(II) hydrate ($Na_2PtCl_4 \cdot xH_2O$, 99.95%, metal base 42.4%, Alfa Aesar), sodium tetrachloropalladate (II) hydrate ($Na_2PdCl_4 \cdot xH_2O$, 99.95%, metal base 30%, Alfa Aesar), and copper chloride dihydrate ($CuCl_2 \cdot 2H_2O$, 99%, Acros Organics) were used as received without further purification.

Synthesis of single-phase MPEA nanoparticles. In a typical synthesis of single-phase AuPtPdCu MPEA colloidal nanoparticles, a stocked oil phase suspension was prepared by mixing 48 mL cyclohexane (with freezing point of ~6.5 ºC), 8 mL n-butanol, and 4 g CTAB with the assistance of ultrasonication for 30 min until the liquid mixture was emulsified to a milky white emulsion. To an Anton Paar G10 microwave reactor tube was sequentially added 20 μL of 0.1 M $HAuCl_4$ aqueous solution, 20 μL of 0.1 M Na_2PtCl_4 aqueous solution, 20 μL of 0.1 M Na_2PdCl_4 aqueous solution, 20 μL of 0.1 M $CuCl_2$ aqueous solution, and 2 mL of the stocked hexane/butanol/CTAB emulsion. The mixture was then sonicated for 15 min and it turned to a clear and orange solution. Such change in appearance was ascribed to the formation of water-in-oil microemulsion micelle vesicles encapsulating the aqueous solution of metal precursors. This solution was denoted as solution **I**. A same procedure was used to prepare a solution containing reducing agent that can reduce metal precursors to synthesize metal nanoparticles. Mixing 2 mL of the stocked hexane/butanol/CTAB emulsion with 80 μL hydrazine hydrate (64% hydrazine) followed by ultrasonication for 15 min led to the formation of water-in-oil microemulsion micelle vesicles encapsulating hydrazine. This solution was denoted as solution **II**. The reaction tube with solution **I** was placed in a freezer that set to –20 °C to freeze solution **I** into a wax-like solid, while solution **II** was stored at the room temperature. Carefully adding the (liquid) solution **II** to the (solid) solution **I** resulted in two layers of well-separated water-in-oil microemulsion solution, preventing the direct contact and reaction between metal precursors and hydrazine. The reaction tube was sealed by a cap with a silicone septum and was then placed in the Anton Paar Monowave 300 microwave reactor. The microwave reactor is equipped with a microwave generator at 2.45 GHz (corresponding to a wavelength of 12.25 cm) and with a maximum power of 850W. The microwave reactor was programmed to deliver a 10-s microwave pulse to the reaction solution at the maximum power (850W). The internal contactless IR thermometer and pressure gauge were used to monitor the global temperature of the reaction solution and gaseous pressure above the reaction solution, respectively. In a typical synthesis, the temperature increased from 0 °C to ~70 °C. Once the microwave was turned off, pressurized air flow was used to promote rapid quenching of the reaction solution. The solution turned to black after reaction, indicating the formation of metal nanoparticles. Centrifuging the solution settled the nanoparticles to the bottom of the centrifuge tube. Washing the settled nanoparticles with ethanol and water three times to remove excess freestanding CTAB. The nanoparticles were then redispersed in ethanol for characterizations. Single-phase MPEA nanoparticles of ternary metal elements were synthesized by following the same procedure except the quantity of metal precursors, which are listed in Table S1.

Address correspondence to ygsun@temple.edu

Table S1 Composition of reaction solutions for synthesizing single-phase MPEA nanoparticles

MPEA Sample	Solution **I**					Solution **II**	
	$HAuCl_4$ /μL	Na_2PtCl_4 /μL	Na_2PdCl_4 /μL	$CuCl_2$ /μL	oil phase emulsion /mL	hydrazine /μL	oil phase emulsion /mL
AuPtPdCu	20	20	20	20	2	80	2
AuPdCu	20	0	20	20	2	60	2
AuPtCu	20	20	0	20	2	60	2
AuPtPd	20	20	20	0	2	60	2
PtPdCu	0	20	20	20	2	60	2

Concentration of each stock aqueous solution of metal precursor was 0.1 M. The concentration of hydrazine was 68%.

Characterization. The synthesized MPEA nanoparticles were examined with high-energy x-ray diffraction (HE-XRD), which was carried out at high energy beamline 11-ID-C at Advanced Photon Source (APS), Argonne National Laboratory (ANL). The wavelength of x-ray was 0.2115 Å, corresponding to photon energy of 58.621 keV. The nanoparticle powders were sandwiched and sealed with Kapton® tape and measured at the high energy beamline. The scattering signals were collected by an imaging plate detector with a resolution of 2048×2048 pixels. The sample-to-detector distance (994.7 mm) was calibrated by fitting the HE-XRD pattern of a standard CeO_2 sample. The recorded 2D scattering patterns were reduced to 1D XRD curves using Fit2D software along with the background subtraction and intensity normalization. A JEOL1400 transmission electron microscope was used to characterize morphology, size, and size distribution of the synthesized nanoparticles. Elemental analysis of ensembled nanoparticles on a silicon substrate was conducted with energy-dispersive x-ray spectroscopy (EDX) using the X-Max^N 50 spectrometer (Oxford instruments) coupled with a FEI QUANTA 450 scanning electron microscope (SEM). The SEM-EDX data was analyzed using the instrument build-in AZtec® software with factory standards. High-resolution TEM and high-angle annular dark-field scanning TEM (HAADF-STEM) images and EDX elemental mapping were performed using an FEI Talos microscope operated at 200kV, which is located at the Center for Nanoscale Materials, ANL.

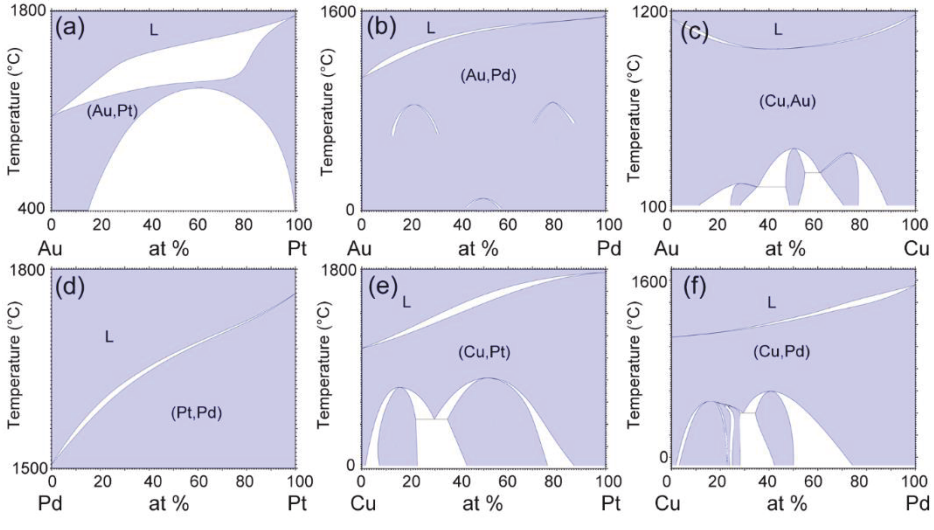

Figure S1 Phase diagrams of binary metal alloys of Au, Pt, Pd, and Cu, showing the thermodynamic miscibility of these metals as a function of compositions and temperatures. (a) The phase diagram of Au-Pt exhibits a large miscibility gap (i.e., immiscibility) at room temperature, indicating the difficulties of forming single phase AuPt alloy. (b-f) Other metal combinations are generally miscible for a broad range of compositions but tend to form meta-stable intermetallic phases at room temperature. Data obtained from ASM Alloy Phase Diagram Database™.

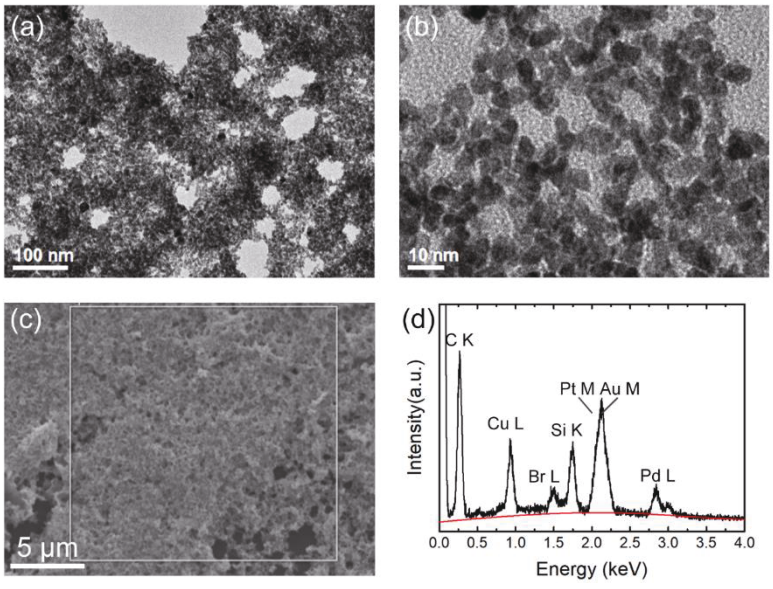

Figure S2 (a) Low-magnification and (b) high-magnification TEM images of the synthesized single-phase AuPtPdCu MPEA nanoparticles dispersed on a TEM grid. (c) Large field-of-view SEM image of the nanoparticles on a silicon substrate and (d) EDX spectrum recorded from the nanoparticles highlighted in the squared in (c). The red curve is the fitted baseline.

Table S2 Analysis of the EDX spectrum of the single-phase AuPtPdCu MPEA nanoparticles

Element	Energy line	Center /keV	Height /counts	Area /count·keV	fwhm /keV	Intensity correction*	**Atomic%***
Cu	L series	0.930	177	18.6	0.0688	0.72	35
Pd	L series	2.838	69	5.6	0.0501	0.88	23
Pt	M series	2.048	261	39.2	0.1405	0.91	17
Au	M series	2.120				0.90	25

*Calculated by the instrument build-in AZtec® quantitative analysis with factory standards.

Table S3 Analysis of HE-XRD peaks

	2θ (111) /°	fwhm /°	Grain size /nm	2θ (200) /°	fwhm /°	Grain size /nm	2θ (220) /°	fwhm /°	Grain size /nm
AuPtPdCu	5.409	0.3104	3.7	6.204	0.5809	2.0	8.839	0.4277	2.7
AuPdCu	5.420	0.2685	4.2	6.227	0.5563	2.1	8.861	0.3941	2.9
AuPtCu	5.408	0.3505	3.3	6.193	0.4951	2.3	8.828	0.5045	2.3
AuPtPd	5.297	0.2309	4.9	6.104	0.3080	3.7	8.648	0.2877	4.0
PtPdCu	5.543	0.4275	2.7	6.294	0.4402	2.6	9.029	0.5903	1.9

fwhm = full width at half maximum; grain sizes were calculated using Scherrer's equation.

Table S4 Interplanar distance along <111>, <200>, <220> and <311> crystalline directions

MPEA nanoparticles	d_{111} /Å	d_{200} /Å	d_{220} /Å	d_{311} /Å	d_{200}/d_{111}	d_{220}/d_{111}	d_{311}/d_{111}
AuPtPdCu	2.242	1.954	1.371	1.172	0.8715	0.6115	0.5227
AuPdCu	2.237	1.944	1.369	1.169	0.8690	0.6120	0.5226
AuPtCu	2.246	1.958	1.376	1.175	0.8718	0.6126	0.5232
AuPtPd	2.294	1.990	1.406	1.198	0.8675	0.6129	0.5222
PtPdCu	2.192	1.920	1.342	1.144	0.8759	0.6122	0.5219

The values were determined from the peaks of HE-XRD patterns.

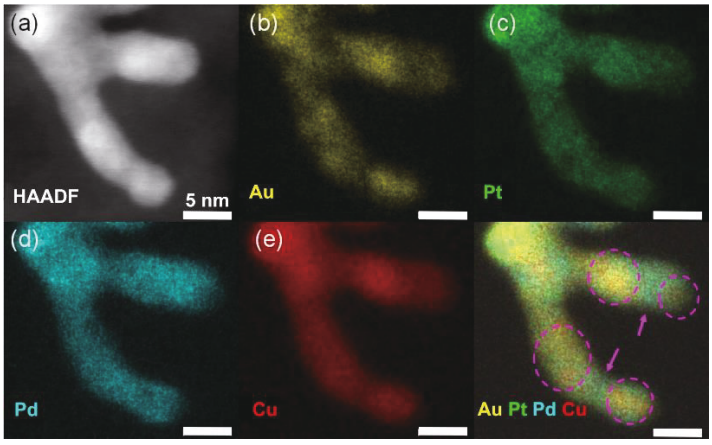

Figure S3 (a) HAADF-STEM image and (b-e) elemental EDX mappings of (b) Au, (c) Pt, (d) Pd, and (e) Cu of the bottlenecks (highlighted by pink arrow) between neighboring nanoparticles (highlighted by dashed pink circles). (f) Overlaid images of the elemental EDX mapping shown in (b-e). The scale bar in (a) also applies to (b-f).

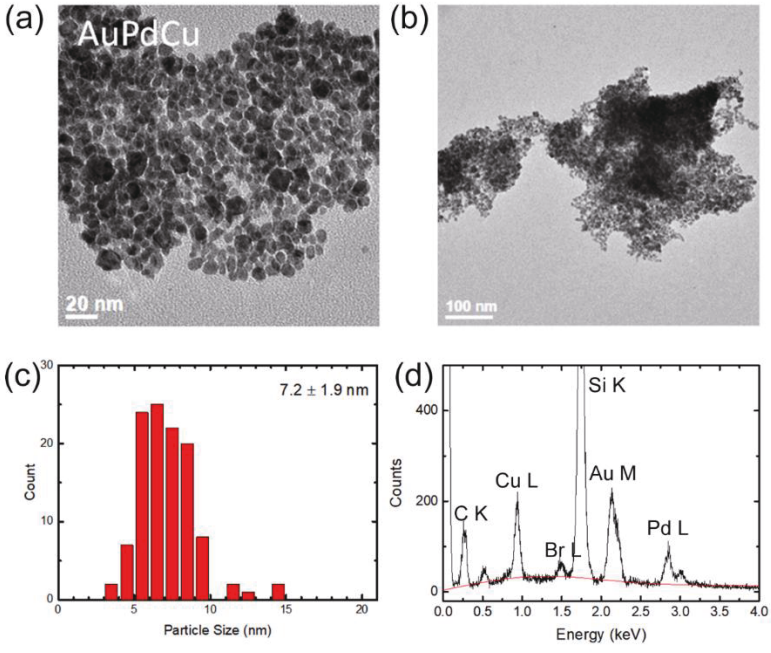

Figure S4 (a, b) TEM image of the synthesized single-phase AuPdCu MPEA nanoparticles dispersed on a TEM grid. (c) Particle size distribution histogram derived from statistic evaluation of the dimensions measured from the TEM image. (d) EDX spectrum of the nanoparticles dispersed on a silicon substrate. The red curve is the fitted baseline.

Table S5 Analysis of the EDX spectrum of the single-phase AuPdCu MPEA nanoparticles

Element	Energy line	Center /keV	Height /counts	Area /count·keV	fwhm /keV	Intensity correction*	**Atomic%***
Cu	L series	0.930	190	12.7	0.0617	0.71	42.1
Pd	L series	2.838	96	7.7	0.0437	0.88	27.9
Pt	M series	2.048	205	25.1	0.1014	0.88	0.1
Au	M series	2.120				0.89	29.9

*Calculated by the instrument build-in AZtec® quantitative analysis with factory standards.

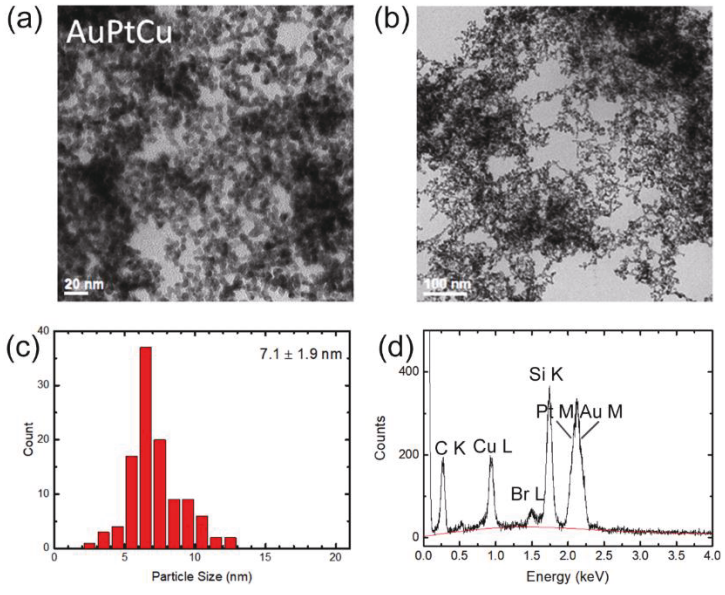

Figure S5 (a, b) TEM image of the synthesized single-phase AuPtCu MPEA nanoparticles dispersed on a TEM grid. (c) Particle size distribution histogram derived from statistic evaluation of the dimensions measured from the TEM image. (d) EDX spectrum of the nanoparticles dispersed on a silicon substrate. The red curve is the fitted baseline.

Table S6 Analysis of the EDX spectrum of the single-phase AuPtCu MPEA nanoparticles

Element	Energy line	Center /keV	Height /counts	Area /count·keV	fwhm /keV	Intensity correction*	**Atomic%***
Cu	L series	0.930	176	16.0	0.0690	0.78	42.6
Pd	L series	2.838	0	0	-	0.86	0.2
Pt	M series	2.048	315	48.5	0.1341	0.93	22.5
Au	M series	2.120				0.91	34.8

*Calculated by the instrument build-in AZtec® quantitative analysis with factory standards.

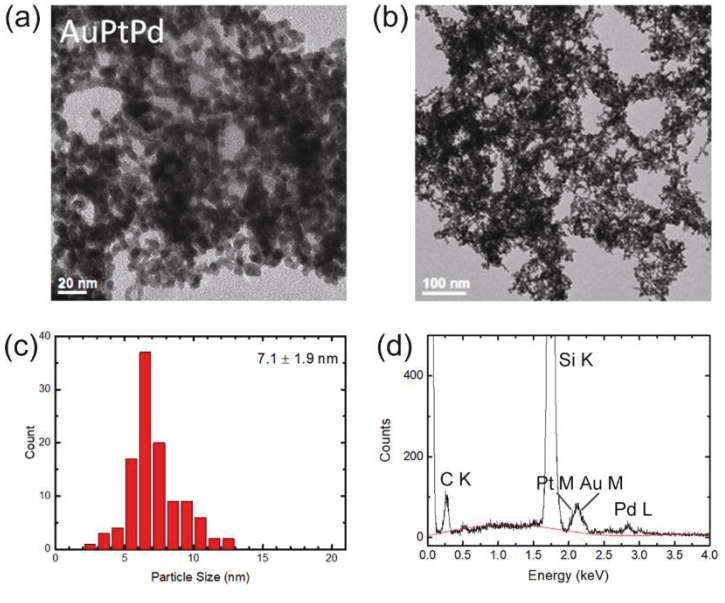

Figure S6 (a, b) TEM image of the synthesized single-phase AuPtPd MPEA nanoparticles dispersed on a TEM grid. (c) Particle size distribution histogram derived from statistic evaluation of the dimensions measured from the TEM image. (d) EDX spectrum of the nanoparticles dispersed on a silicon substrate. The red curve is the fitted baseline.

Table S7 Analysis of the EDX spectrum of the single-phase AuPtPd MPEA nanoparticles

Element	Energy line	Center /keV	Height /counts	Area /count·keV	fwhm /keV	Intensity correction*	**Atomic%***
Cu	L series	0.930	0	0	-	0.68	0.0
Pd	L series	2.838	36	3.1	0.0352	0.89	41.3
Pt	M series	2.048	74	10.3	0.1129	0.96	23.4
Au	M series	2.120				0.94	35.3

*Calculated by the instrument build-in AZtec® quantitative analysis with factory standards.

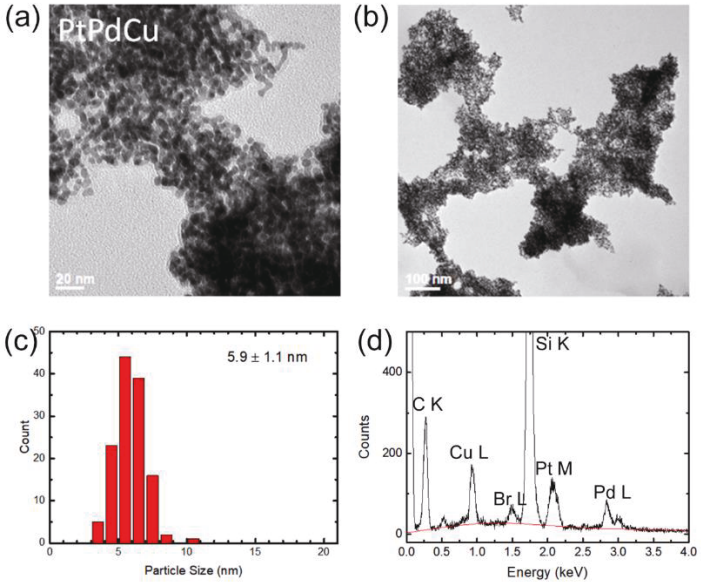

Figure S7 TEM image of the synthesized single-phase PtPdCu MPEA nanoparticles dispersed on a TEM grid: (a) zoom out, (b) zoom in. (c) Particle size distribution statistics according to the dimensions measured from the TEM image (d) EDX spectrum of the nanoparticles dispersed on a silicon substrate, the red curve is the fitted baseline.

Table S8 Analysis of the EDX spectrum of the single-phase PtPdCu MPEA nanoparticles

Element	Energy line	Center /keV	Height /counts	Area /count·keV	fwhm /keV	Intensity correction*	**Atomic%***
Cu	L series	0.930	148	11.8	0.0766	0.71	47.6
Pd	L series	2.838	73	6.3	0.0661	0.90	31.1
Pt	M series	2.048	120	13.8	0.0924	0.85	21.3
Au	M series	2.120				0.84	0.0

*Calculated by the instrument build-in AZtec® quantitative analysis with factory standards

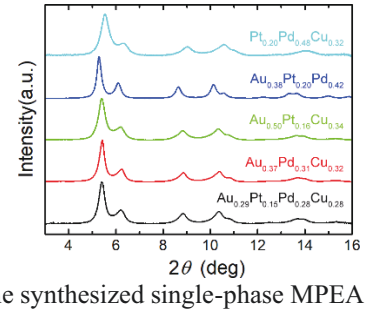

Figure S8 Full range HE-XRD patterns of the synthesized single-phase MPEA nanoparticles made of $Au_{0.29}Pt_{0.15}Pd_{0.28}Cu_{0.28}$, $Au_{0.37}Pd_{0.31}Cu_{0.32}$, $Au_{0.50}Pt_{0.16}Cu_{0.34}$, $Au_{0.38}Pt_{0.20}Pd_{0.42}$, and $Pt_{0.20}Pd_{0.48}Cu_{0.32}$.